



# UNIVERSITÀ DI PARMA

## ARCHIVIO DELLA RICERCA

University of Parma Research Repository

The adaptation of lipid profile of human fibroblasts to alginate 2D films and 3D printed scaffolds

This is the peer reviewed version of the following article:

*Original*

The adaptation of lipid profile of human fibroblasts to alginate 2D films and 3D printed scaffolds / Zanotti, I.; Marando, S.; Remaggi, G.; Bergonzi, C.; Bernini, F.; Bettini, R.; Elviri, L.. - In: BIOCHIMICA ET BIOPHYSICA ACTA-GENERAL SUBJECTS. - ISSN 0304-4165. - 1865:1(2021), p. 129734. [10.1016/j.bbagen.2020.129734]

*Availability:*

This version is available at: 11381/2881578 since: 2021-12-20T10:36:00Z

*Publisher:*

Elsevier B.V.

*Published*

DOI:10.1016/j.bbagen.2020.129734

*Terms of use:*

Anyone can freely access the full text of works made available as "Open Access". Works made available

*Publisher copyright*

note finali coverpage

(Article begins on next page)

13 May 2024

1 **The adaptation of lipid profile of human fibroblasts to alginate 2D films and 3D**  
2 **printed scaffolds**

3  
4 Ilaria Zanotti, Silvia Marando, Giulia Remaggi, Carlo Bergonzi, Franco Bernini, Ruggero Bettini,  
5 Lisa Elviri\*

6  
7 <sup>1</sup>Department of Food and Drug Science, University of Parma, Parco Area delle Scienze 27/A, 43124,  
8 Parma, Italy.

9  
10  
11 \* Corresponding Author: Prof. PhD Lisa Elviri

12 Phone: +39 0521 905087

13 Fax: +39 0521 905006

14 E-mail: [lisa.elviri@unipr.it](mailto:lisa.elviri@unipr.it)

15

16

17

18

19

20

21

22

23

24

25

26

27 **Highlights**

- 28 • 2D films and 3D printed scaffolds from alginate
- 29 • LC-MS/MS lipid investigation on ALG action mechanism on fibroblasts
- 30 • Ceramides modulation after cell-biomaterial interactions

31

32

33

34

35

36

37

38

39

40

41

42

43

44

45

46

47

48

49

50

51

52

53

## 54 **Abstract**

55 Background: The investigation of the interactions between cells and innovative, active material is  
56 pivotal in the emerging 3D printing-biomaterial application fields. Here, lipidomics has been used to  
57 explore the early impact of alginate (ALG) hydrogel architecture (2D films or 3D printed scaffolds)  
58 and the type of gelling agent ( $\text{CaCl}_2$  or  $\text{FeCl}_3$ ) on the lipid profile of human fibroblasts.

59 Methods: 2D and 3D ALG scaffolds (2D\_ and 3D\_ALG) were prepared and characterized in terms of  
60 water content, swelling, mechanical resistance and morphology through SEM analysis before human  
61 fibroblast seeding (8 days). Using a liquid chromatography-triple quadrupole-tandem mass  
62 spectrometry approach, selected ceramides (CER), lysophosphatidylcholines (LPC),  
63 lysophosphatidic acids (LPA) and free fatty acids (FFA) were analyzed.

64 Results: The results showed a clear alteration in the CER expression profile depending of both the  
65 geometry and the gelling agent used to prepare the hydrogels. As for LPCs, the main parameter  
66 affecting their distribution is the scaffold architecture with a significant decrease in the relative  
67 expression levels of the species with higher chain length (C20 to C22) for 3D scaffolds compared to  
68 2D films. In the case of FFAs and LPAs, only slight differences were observed as a function of  
69 scaffold geometry or gelling agent.

70 Conclusions: Variations in the cell membrane lipid profile were observed for 3D cell cultures  
71 compared to 2D and these data are consistent with activation processes occurring through the  
72 mutual interactions between fibroblasts and ALG support. These unknown physiologically relevant  
73 changes add insights into the discussion about the relationship between biomaterial and the  
74 variations of cell biological functions.

75

76

## 77 **Keywords**

78 Ceramides, fatty acids, lysophosphatidic acids, lysophosphatidylcholines, human fibroblasts, 3D  
79 printing, alginate, liquid chromatography-mass spectrometry

80

81

## 82 **1. Introduction**

83 In the recent years the development of innovative active materials in combination with new  
84 production technologies (i.e. micro- and nano-systems, 3D printing, electrospinning, etc.) is of  
85 growing interest in several research and application fields (i.e. drug delivery, regenerative medicine,  
86 gene therapy, *in vitro* diagnostic tests, etc.) [1-3]. The driving idea is to overcome essential limitations  
87 of traditional approaches (i.e. introduction of more reliable diagnostic tests, improvement of drug  
88 delivery systems, bio-fabrication of tissues or organ-like systems etc.), and many efforts are made to  
89 evaluate the effectiveness of these systems through *in vitro* and *in vivo* studies.

90 In such a context, the investigation of the interactions between cells and biomaterials- is pivotal to  
91 obtain a more comprehensive mechanistic understanding of the cause-effect relationships of the  
92 whole system. The capability to offer thorough pictures of these complex living processes allow to  
93 drive new development strategies in the huge application landscape of biomaterials. However, many  
94 challenges still remain open, as it is well known that cell behavior depends upon several factors,  
95 including microenvironment dimensions, structure and chemico-physical composition.

96 Biomaterials interact with the cells at various length scales, from that of individual cells  
97 (micrometers) to the that (nanometers) of single molecules (i.e. proteins, lipids). These interactions  
98 are based on both physical contact and chemical binding and depend over time as a function of the  
99 dimension of the system. Individual cells interact via integrin with a biomaterial for days or weeks,  
100 while individual proteins, or lipids or glycosaminoglycans interact through secondary bonds and  
101 hydrophobic interactions on time scales as short as seconds and minutes [4, 5]. A complex network  
102 of non-covalent kinetically rapid interactions such as hydrogen bonds, van der Waals and  
103 hydrophobic interactions can affect the more driving and thermodynamically stable ionic interactions.

104 The spatial architecture, surface area, interstitial pore distribution and dimensions of native  
105 extracellular matrix (ECM) strongly influence the cell migration, proliferation and differentiation [6].  
106 Biomaterial surfaces can induce changes either in the cell membrane fluidity and permeability, which  
107 in turn regulate cellular and tissue functions, or in cell phenotype, including morphology,  
108 proliferation and biochemical properties [7, 8]. For example, the surface and inner pore size of a  
109 scaffold influence the migration speed of cells: in collagen-GAG scaffolds the smaller is the average  
110 pore size, the lower is fibroblast migration speed [9-11]. Nonetheless, it has been shown that prostate  
111 cancer cells migrate faster than fibroblasts through the same scaffold [12]. It is clear that the  
112 knowledge of these effects at the molecular level can help to develop and tune optimal biomaterials  
113 and scaffolds as a function of the application.

114 Alginate (ALG) is a widely investigated biomaterial used in drug delivery and in many biomedical  
115 applications thanks to its excellent properties, such as biocompatibility, low toxicity, low cost and  
116 ability to undergo spontaneous gelation under mild conditions [13-16]. ALG is a natural occurring  
117 anionic polymer extracted from the brown algae cell wall. It is an unbranched binary copolymer  
118 consisting of the repetition of the monomer units D-mannuronic acid (M) and L-glucuronic acid (G),  
119 held together by  $\beta$ 1-4 bonds [17]. During ionotropic gelation a network of interactions involving  
120 different junction zones (i.e. -OH,  $\text{COO}^-$  and  $-\text{O}^-$  groups) of consecutive G-residues of the ALG chains  
121 and the cation occurs. Calcium chloride ( $\text{CaCl}_2$ ) represents one of the most used crosslinking agent  
122 for the formation of the ALG ionotropic hydrogel. The divalent cations bind only to the glucuronic  
123 acid blocks of the ALG chains forming a cross-linking model called "egg-box", resulting in a gel  
124 structure. Conversely, chelation with the trivalent  $\text{Fe}^{3+}$  ions allows for more spherical shapes [18]. In  
125 general, the speed of gelation is an important parameter to control the uniformity and shape of the  
126 gel. Slower gelation leads to the production of more uniform structures and greater mechanical  
127 integrity [19]. Furthermore, better cell adhesion and proliferation have been observed on ALG  
128 matrices when the latter is gelled with trivalent ions, such as  $\text{Fe}^{3+}$  [20]. ALG, as cross-linked hydrogel  
129 deriving from a natural polysaccharide, presents structure, flexibility, porosity and diffusive transport

130 characteristics similar to the ECM of human native tissues and is used in regenerative medicine as  
131 dressings to keep a wound moist, minimize bacterial infection and accelerate the healing process [18].  
132 Among applications ALG is widely exploited for the controlled release of drugs and proteins, for the  
133 transport of cells to a specific site [21-23] and to perform two-dimensional (2D) and three  
134 dimensional (3D) cell studies to understand cell-matrix interactions.

135 Although cells in a living system are exposed to complex 3D biological environments, biological  
136 phenomena is still extensively investigated by means of 2D substrates. 2D assays present major  
137 limitations to accurately describe the space constraints of cells *in vivo* and can induce different cell  
138 activities and/or loss of the original cell phenotype. 2D films are still widely used in several cell  
139 culture experiments, but 3D printing manufacturing process is rapidly gaining a prominent role as  
140 innovative technology in the medical or diagnostic fields to shape biopolymers in a variety of  
141 architectures to progressively replace two dimensional systems [24-29].

142 With the aim to improve the basic knowledge available in the cell-biomaterial interaction field, in  
143 this study the effects of different architectures and gelling media used for the preparation of ALG  
144 hydrogels were investigated for the first time on the targeted lipid profile of human fibroblasts.  
145 Controlled and reproducible 2D films (2D-ALG) and 3D printed ALG scaffolds (3D-ALG) were  
146 produced by gelation with  $\text{CaCl}_2$  or iron chloride ( $\text{FeCl}_3$ ), and a selected targeted lipid profile of  
147 human fibroblasts seeded on them was evaluated. Cell biochemistry can be studied at different  
148 complementary levels (i.e. the transcriptome, proteome, lipidome or metabolome) to gain information  
149 useful to frame their behavior [30, 31]. Here we decide to focus our attention on lipids, as they play  
150 a crucial role in the physiology of cells, tissues and organs as demonstrated by a large number of  
151 genetic studies [32]. The deregulation of lipid metabolic pathways therefore leads to the onset of  
152 diseases, including cardiovascular disorders, cancer and diabetes [33-35].

153 Lipidomics is nowadays a consolidated field capable of a comprehensive analysis of lipids in complex  
154 biological systems. Lipidomics aims to profile the lipid structures and quantity in a biological sample,  
155 to assess their metabolic functions and transformations that occur in different physiological and

156 pathological conditions [36]. The birth of lipidomics has been possible thanks to technological  
157 advances in the field of analytical instrumentation such as mass spectrometry (MS) [37-39]. This set  
158 of techniques is the golden standard approach for the investigation of the lipids in cells by virtue of  
159 their ability to perform the simultaneous identification and quantification of thousands of analytes in  
160 the same biological sample. Here a liquid chromatography-electrospray-tandem mass spectrometer,  
161 with a triple quadrupole mass analyzer, was used for the identification and relative quantitative  
162 detection of lipids belonging to the following classes, selected as powerful mediators of cell  
163 functions: ceramides (CER), fatty acids (FFA), lysophosphatidic acids (LPA) and  
164 lysophosphatidylcholines (LPC). CER and FFA are lipid species that modulate membrane rigidity,  
165 creating micro-domains, and altering membrane permeability, thus regulating cell membrane  
166 functions [40]. Moreover, CER enhance the bioavailability of drugs by acting as lipid delivery  
167 systems, they play a structural role in liposome formulations and enhance the cellular uptake of  
168 amphiphilic drugs, such as chemotherapeutics [41]. In a recent study FFA have been chemically linked  
169 with biological drug molecules to enhance oral absorption of therapeutic peptides and to provide a  
170 platform for oral peptide drug development [42]. LPA derivatives are bioactive phospholipids present  
171 in biological fluids that regulate many important fibroblast functions, including proliferation,  
172 migration and contraction. Alteration in normal LPA signaling may contribute to a range of diseases,  
173 including neurodevelopmental and neuropsychiatric disorders, pain, cardiovascular disease, bone  
174 disorders, fibrosis, cancer, infertility, and obesity [43]. Therefore, therapies targeting LPA  
175 biosynthesis and signalling may be feasible for the treatment of devastating human diseases [44].  
176 LPC are present as minor phospholipids in the cell membrane and blood plasma, promote  
177 inflammatory effects [45] and play a role in the pathway of fibrotic injury in human cardiac fibroblasts  
178 [46].

179

## 180 **2. Materials and methods**

### 181 **2.1. Reagents**

182 Acetonitrile, methanol, hexane and isopropanol were supplied from Sigma-Aldrich (Taufkirchen,  
183 Germany). Water was purified (0.055 uS/cm, TOC 1ppb) with a Purelab pulse + Flex ultra-pure water  
184 system (Elga Veolia, Milan, Italy).

185

## 186 **2.2. Scaffold preparation**

187 ALG formulation (Ph.Eur. grade; molecular weight by gel filtration chromatography (GFC) 180–300  
188 kDa; slowly soluble in water, Carlo Erba, Italy) was prepared by dissolving the sodium ALG 6%  
189 (w/v) in deionized water. The formulation was left under stirring overnight on a magnetic plate until  
190 a homogeneous mixture was obtained. The ALG films (2D scaffolds) were obtained by pouring the  
191 6% ALG formulation onto a glass plate and then stretching it using a 0.6mm film-stretcher. The two  
192 casting solutions were left to dry in an oven at 40 °C for minutes and 2 and a half hours, respectively.  
193 At this point, the dried alginate films were immersed in the solutions of CaCl<sub>2</sub> 3% (w/v), (anhydrous  
194 CaCl<sub>2</sub>, lot. 419887/1, Fluka Chemie GmbH, Switzerland) or FeCl<sub>3</sub> 3% (w/v), (anhydrous FeCl<sub>3</sub> 98%,  
195 lot. H29Y005, Alfa Aesar, United States) to cross-link for one hour. Subsequently, films were  
196 detached from the glass plates and rinsed twice in deionized water for 15 min.

197 The 3D ALG scaffolds were made by using a 3D printer built in house (38). The machine is based on  
198 a three cartesian axes system that allows the movement on the horizontal plane of printing plate and  
199 the vertical translation of the nozzle. ALG solution was loaded into a 10 ml syringe and was extruded  
200 by a pump acting on a syringe mounting a 26G needle, deposited, layer by layer, on the printing plate  
201 at a velocity of 3 mm/s and instantaneously frozen (-14 °C) with a series of Peltier cells which allows  
202 the material, to freeze instantly and maintain the three-dimensional structure. At the end of the print,  
203 the steel plate with the scaffold is removed and immersed in the gelling solution (CaCl<sub>2</sub> 3% (w/v) or  
204 FeCl<sub>3</sub> 3% (w/v)) for one hour. At the end of the gelling process, the scaffold is rinsed in deionized  
205 water to remove all traces of the gelling agent.

206

## 207 **2.3. Evaluation of water content**

208 To determine the water content, 3D (5-layer square with a side of 1.4 cm) and 2D (2mm-thick) ALG  
209 scaffolds gelled in CaCl<sub>2</sub> (ALG\_Ca) or in FeCl<sub>3</sub> (ALG\_Fe) were prepared. After being molded, the  
210 scaffolds were gelled for 1 hour in the respective gelling agents and subsequently rinsed in deionized  
211 water. The scaffolds were lightly buffered on absorbent paper and weighed on an analytical balance  
212 to determine the wet weight (W<sub>w</sub>). Subsequently, the scaffolds were dried in an oven at 40 °C  
213 overnight and weighed again to determine their dry weight (W<sub>d</sub>). Five replicates were analyzed. The  
214 water content (W<sub>c</sub>) was calculated as:

$$215 \quad Wc = \frac{(Ww - Wd)}{Ww * 100}$$

216

#### 217 **2.4. Swelling test**

218 The swelling behavior of the scaffolds was evaluated over time (1 min, 30 min, 1h, 2h, 6h, 24 hours)  
219 by measuring their weight. To perform the test, 5-layer square ALG scaffolds were created, with a  
220 side of 1.4 cm. After printing, the scaffolds were gelled for 1 hour in the respective gelling agents  
221 and subsequently rinsed in deionized water and dried in an oven at 40 °C overnight before weight  
222 measurement. Subsequently, each scaffold was placed in deionized water and the weights were taken  
223 at each time interval. Before each measurement, the scaffolds were swabbed on absorbent paper to  
224 eliminate surface drops. Five replicates were analyzed. The swelling ratio (Q<sub>s</sub>), defined as the average  
225 percentage of swelling, was assessed through the following equation:

$$226 \quad Qs = \frac{(Ws - Wd)}{Wd}$$

227 where W<sub>s</sub> represents the weight of the scaffold at a certain time and W<sub>d</sub> is its initial weight.

228

#### 229 **2.5. Mechanical properties**

230 The mechanical resistance of ALG\_Ca or ALG\_Fe was measured by using 3D 20-layers scaffolds  
231 and 2mm-thick ALG films having size of 5 cm x 1.5 cm. Thickness was determined (n. of replicates  
232 = 6) with a digital micrometer (Mitutoyo, Japan). Each scaffold was fixed on a tensile tester (AG M1

233 Acquati, Italy) loaded with a 5 daN cell. Force and time signals were digitalized by means of a  
234 PowerLab 400 board and recorded with the Scope v.3.5 software. Elongation at break (% strain) and  
235 Young's modulus were determined from the relevant stress-strain curves, taking into consideration  
236 the linear portion. Three replicates were analyzed.

237

## 238 **2.6. SEM analysis**

239 SEM analysis were carried out to study the morphology and pore distribution of 2D\_ALG and  
240 3D\_ALG . 2D\_ALG (n=3) or 3D\_ALG 10-layers square (1.5x1.5 cm)gelled in CaCl<sub>2</sub> or in FeCl<sub>3</sub>  
241 were prepared . The samples were immersed in increasing concentrations of ethanol (10%, 20%, 30%,  
242 40%, v/v in dH<sub>2</sub>O) 10 minutes for each step. Subsequently, the samples were subjected to freeze-  
243 drying for 24 hours in the Christ Alpha 2-4 LSC plus Freeze Dryer and gold sputtered through a  
244 metallizer (Balzers). Surface and section images of 3D samples were captured at different  
245 magnifications, ranging from 80X to 640X. Photographs of 2D film surfaces were acquired at 300X  
246 magnification. For the acquisition of the images of 2D\_ALG a scanning electron microscope (Sigma  
247 HD, Carl Zeiss, Jena, Germany) at EHT 1.00 kV was used while a SEM 501 (Philips) was employed  
248 for 3D scaffold characterization. All images were analyzed by ImageJ software (NIH, Bethesda USA)  
249 for the measurement of macro- and micro-structures, mean pore size (Feret diameter) and distribution.

250

## 251 **2.7. Cell culture**

252 Primary human skin fibroblasts, coded as C86, were derived from a forearm biopsy of a healthy donor  
253 after signature of an informed consent. Cells were maintained in Dulbecco's Modified Eagle's  
254 Medium (DMEM, Gibco) culture medium, supplemented with 1% (v/v) of L-glutamine (Gibco), 1%  
255 of Streptomycin and Penicillin (Gibco), 1% of Na-pyruvate (Gibco), 1% of NEAA (Non-Essential  
256 AminoAcids, Gibco) and 10% of FBS (Fetal Serum Bovine, Euroclone). After overnight disinfection  
257 in ethanol 70 % (v/v in dH<sub>2</sub>O), 2D\_ALG and 3D\_ALG were deposited in 12-well plates (Constar)

258 and washed with sterile water. The following conditions have been tested: positive control  
259 (represented by the seeding of cells directly in the well); 2D\_ALG\_Ca; 3D\_ALG\_Ca ; 2D\_ALG\_Fe;  
260 3D\_ALG\_Fe ; negative control (represented by films and scaffolds without cells).

261 500k cells per well were seeded (150  $\mu$ l) directly on 2D and 3D scaffolds to observe the impact of  
262 microenvironment on cell behavior and 850  $\mu$ l of 10% FCS medium were added to reach the volume  
263 of 1 ml. Cells were incubated and maintained for 8 days at 37° C, 5% CO<sub>2</sub> (Incubator Nabco,  
264 Chicago, IL, USA).

265

## 266 **2.8. MTT assay**

267 The MTT assay was carried out as follows: 500  $\mu$ l of a solution consisting of MTT (1 mg/ml) and 5%  
268 FCS medium were added to each well. The cells were incubated for 2h at 37 °C. After two hours, the  
269 MTT and medium solution was aspirated and the films and scaffolds were transferred into new plates.  
270 500 $\mu$ l of DMSO (dimethylsulfoxide) were added to each well and the plates were stirred on a tilting  
271 plate for 15-20 minutes at room temperature. From each well 200 $\mu$ l were taken and placed in a 96-  
272 well plate (Constar, Flat Transparent) for spectrophotometric reading. Each sample was analyzed in  
273 duplicated. 200 $\mu$ l of DMSO was added to two wells of the plate to be used as a control.  
274 Spectrophotometry reading was carried out at a wavelength of 570 nm. The spectrophotometer used  
275 is a TECAN Spark 10M spectrophotometer. The data relating to the analysis were processed by  
276 subtracting the absorbances obtained from the cell-free supports (negative controls).

277

## 278 **2.9. Lipid extraction**

279 The extraction of lipids from cellular matrices was performed by using a mixture of hexane and  
280 isopropanol (3:2; v/v). Cells grown on plastic and ALG films were detached using trypsin, centrifuged  
281 and resuspended in iced sterile water. To detach the cells grown on the 3D scaffolds an EDTA-Na  
282 citrate (EDTA 50 mM; Na citrate 55 mM) solution was used to dissolve the scaffolds. The contents  
283 of the wells were centrifuged and the pellet was resuspended in iced sterile water. The cell suspension

284 obtained was transferred to cryotubes and cell lysis was obtained by 2 freezing cycles in liquid  
285 nitrogen and thawing at 37 ° C for 10 minutes. Subsequently, the samples were transferred into glass  
286 tubes and 360 µl of hexane and 240 µl of isopropanol were added. After being vortexed for 1 min,  
287 the tubes were centrifuged (2000 rpm x 5 min). The organic phase was transferred to new glass tubes,  
288 and the procedure was repeated twice. The supernatants obtained were evaporated under nitrogen  
289 stream and resuspended in 50 µL of methanol before LC-MS analysis.

290

## 291 **2.10. Liquid chromatography-mass spectrometry analysis**

292 The analyses were carried out by using an HP1200 Agilent LC system (Agilent Technologies, USA)  
293 equipped with an electrospray QTRAP 4000 mass spectrometer (ABSCIEX, CA, USA). The  
294 chromatographic separation was carried out on C18 (50x2.1 mm, 5 µm) column (Phenomenex, CA,  
295 USA). Mobile phase was (A) methanol and (B) acetonitrile. The mobile phase was filtered through a  
296 0.45 µm cellulose membrane before use. Flow-rate was 0.2 mL/min and the injected volume was 10  
297 µL. The system was controlled by the Analyst software v. 1.4. (ABSCIEX). Source parameters were:  
298 negative ion (NI) ESI voltage, -4.5 kV; declustering potential, -50 V; entrance potential, -10V; source  
299 temperature, 350 °C and positive ion (PI) ESI voltage, 5.5 kV; declustering potential, 50 V; entrance  
300 potential, 10V; source temperature, 350 °C. Quadrupoles were tuned to unit resolution. As for  
301 quantitative analysis, experiments were performed under PI- or NI-SRM conditions using nitrogen  
302 as collision gas (medium nitrogen pressure). The SRM transition considered in this study are reported  
303 in the Table 1 of the supplementary material. The analytes were relatively quantified among samples  
304 and normalized for MTT assay. The chromatograms were analyzed through the MultiQuant software  
305 (version 2.1).

306

## 307 **2.11 Statistical analysis**

308 Comparisons between groups were made by one-way ANOVA with Tukey's correction for multiple  
309 testing. The data from LC/MS analysis have been expressed as % of the individual lipid specie on the

310 total amount of lipids on each biomaterial. Given the large number of observations that are highly  
311 correlated with each other, no statistical analysis was made for comparison of lipid species profiles  
312 within the four biomaterials.

313

### 314 **3. Results and discussion**

#### 315 **3.1. 2D\_ALG and 3D\_ALG preparation and characterization**

316 In the first part of the work the preparation and characterization of the 2D\_ALG and 3D\_ALG (Figure  
317 1) were addressed in order to study the effects of the different gelling media on the final hydrogel  
318 properties. In general, ALG presents different chelating affinity for its cross-linking cations, as a  
319 function of their charge and dimensions, resulting in hydrogels having different properties such as  
320 swelling, elasticity and stability.

321 The determination of the water content, a parameter that allows to evaluate the ability of the scaffolds  
322 to absorb biological fluids and keep the tissues hydrated, displayed that both 2D\_ and 3D\_ALG\_Fe  
323 retain very similar percentage of water ( $93\pm 1\%$ ) compared to 2D\_ and 3D\_ALG\_Ca ( $90.1\pm 0.8\%$ ).

324 The swelling tests showed that, in general, ALG\_Ca immersed in deionized water tend to swell up  
325 to 6h. ALG\_Fe, on the other hand, showed this behavior only up to 2h (Figure 2). The ALG scaffolds  
326 were also submitted to stress-strain tests. The maximum stress (MPa) was calculated by dividing the  
327 force applied at the breaking point (N) by the cross section area of the specimens ( $\text{mm}^2$ ). Another test  
328 used was the tensile test that allowed to determine Young's modulus, (modulus of elasticity). The  
329 viscoelastic behavior of the scaffolds was therefore determined.

330 3D\_ALG\_Ca showed greater mechanical strength ( $5.7\pm 1.1$  N) and therefore required greater strength  
331 to be broken, while 3D\_ALG\_Fe scaffolds were less resistant ( $4.9\pm 1.0$  N). 3D\_ALG\_Ca scaffolds  
332 were characterized by greater elasticity ( $6.5 \pm 0.4$  MPa), than 3D\_ALG\_Fe, which were extremely  
333 rigid ( $0.72 \pm 0.05$  MPa). The gelling agent, therefore, caused a change in the elastic behavior of the

334 ALG, making it particularly elastic and resistant when gelled with  $\text{CaCl}_2$  and excessively rigid and  
335 less resistant when crosslinked with  $\text{FeCl}_3$ .

336 2D\_ALG were also characterized for their mechanical behavior. As for 3D\_ALG, a macroscopic  
337 difference in terms of consistence was noticed between samples gelled by the two media. In particular,  
338 2D\_ALG\_Ca appeared stiff but much less rigid compared to 2D\_ALG\_Fe.

339 Measurements showed an average Young's modulus of  $3.3 \pm 1.5$  MPa and  $26 \pm 8$  MPa for  
340 2D\_ALG\_Ca and 2D\_ALG\_Fe, respectively. 2D\_ALG\_Ca showed an elastic behavior only during  
341 the first phase of longitudinal traction, followed by deformation of the samples (plastic behavior) and  
342 consequent rupture. 2D\_ALG\_Fe showed instead a linear increase of stress over strain until breakage,  
343 that occurred very early due to the rigidity of the tested material.

344 The higher elasticity and plasticity of 2D\_ALG\_Ca was demonstrated as well by the calculation of  
345 percent elongation, whose mean value resulted  $20.3 \pm 9.9$  %. In comparison, 2D\_ALG\_Fe showed a  
346 significantly lower strain, with a maximum percent elongation of  $3.0 \pm 1.5$  %. While 2D\_ALG\_Ca  
347 highlighted suitable features for potential adoption as material for regenerative medicine,  
348 2D\_ALG\_Fe demonstrated overall weak mechanical properties, being very rigid, devoid of elasticity  
349 and capability to flex or strain without breakage.

350 As for morphological characterization, SEM analysis was carried out to evaluate the microstructure  
351 of the ALG scaffolds. The scaffolds should have a high porosity and an interconnected pore structure  
352 suitable for penetration, as well as adhesion, proliferation and cell differentiation. Figure 3 displays  
353 the pore size distribution, on surface of 3D\_ALG\_Ca scaffolds (**Figure 3a-b**) and of 3D\_ALG\_Fe  
354 (Figure 3d-e). In the first case the average pore size, expressed as Feret's diameter, was between 11-  
355 45  $\mu\text{m}$ ; while in the second case the average pore size was higher (between 11-126  $\mu\text{m}$ ). This  
356 difference could be attributed to the gelling agent which leads to the formation of more or less large  
357 pores during the gelation process of the biomaterial. In both cases, the pore size was adequate for the  
358 penetration of fibroblasts which had a diameter ranging from 15 to 20 microns.

359 The longitudinal cross-section of 3D\_ALG\_Ca exhibited high porosity with homogenous distribution  
360 (5-40  $\mu\text{m}$ ) (Figure 3c). 3D\_ALG\_Fe showed regular tubular morphology mimicking a vessel-like  
361 structure (Figure 3f), where the inner diameters of the hollow filaments range from 50  $\mu\text{m}$  to 140  $\mu\text{m}$ .  
362 This morphological behavior strongly depends on the gelling conditions and can be useful to design  
363 scaffolds with tunable shapes for further applications in regenerative medicine or drug delivery. The  
364 differences observed between the effects of the two gelling media can correlate with the differences  
365 between the mechanical properties described above. In fact the 3D\_ALG\_Ca showed greater  
366 mechanical strength, compared to the less resistant 3D\_ALG\_Fe.  
367 2D\_ALG present much less porous compared to 3D\_ALG. Few pores having dimensions of 10 to 20  
368 microns are randomly spread on the surfaces of overall compact structures. 2D\_ALG\_Fe (Figure 3h)  
369 showed the presence of cracks in the polymeric structure, intermitted by rougher and more corrugated  
370 surfaces compared to 2D\_ALG\_Ca (Figure 3g).

371

### 372 **3.2. LC-MS/MS SRM analysis of the fibroblast lipid profile**

373 The expression of CER, LPC, LPA and FFA was evaluated to understand how and if the geometry  
374 of 2D\_ and 3D\_ALG or the gelling agents are able to affect their relative expression levels in dermal  
375 human fibroblasts.

376 Before LC-MS/MS analysis, the viability of the cells in contact with the 2D\_ and 3D\_ALG was  
377 quantitatively assessed after 8 days by MTT colorimetric assay. Biocompatibility was demonstrated  
378 for 2D\_ and 3D\_ALG\_Ca (approx. 70% vs cells grown on Petri dish), and for 2D\_ and 3D\_ALG\_Fe  
379 (approx. 26 % vs cells grown on Petri dish) (Figure 4). In this latter case, a lower vitality percentage  
380 was obtained, but it should be noted that these supports were more difficult to handle because of a  
381 reduced structural stability in the cell culture media. It was observed that the cell culture medium  
382 impacted on the scaffold structure. In particular, ALG\_Fe tended to dissolve in the medium over the  
383 experimental time (images not shown), whereas ALG-Ca retained their structure. Such results could

384 be in agreement with the different mechanical properties of the hydrogels obtained with calcium and  
385 iron or even with the affinity of the substances present in the culture medium toward the cations.

386

### 387 **3.3. Ceramides**

388 Nineteen CER d18:1 containing species were determined by targeted MS analysis. Among them, a  
389 remarkable variability was observed as a function of the scaffold preparation. The results obtained  
390 clearly show that the relative expression of these lipids was significantly affected by both the structure  
391 of the scaffolds and the gelling agents employed (Figure 5).

392 The most abundant species, represented by CER d18:1-16:0 and CER d18:1-22:0, showed a peculiar  
393 expression in response to the structure and the composition of the supports. The former reveals  
394 significantly higher amount on 2D\_ALG\_Ca than on 2D\_ALG\_Fe and on 3D\_ALG\_Ca, while the  
395 opposite was observed in the latter. In addition, CER d18:1-22:0 was more abundant when cells were  
396 grown on 2D\_ALG\_Fe compared to 3D\_ALG\_Fe. In the relatively less expressed species, a well-  
397 defined trend is evident: the short chain ceramides (CER d18:1-16:1, CER d18:1-20:0) present higher  
398 expression on the 2D\_ALG\_Ca compared to 3D\_ALG\_Ca, while the opposite occurs for long chain  
399 ceramides (CER d18:1-22:2, CER d18:1-22:5). The influence of the support composition is evident  
400 for many lipid species, that presented higher abundance on 2D\_ALG\_Ca (CER d18:1-16:0, CER  
401 d18:1-16:1, CER d18:1-20:0, CER d18:1-22:0, CER d18:1-22:2, CER d18:1-22:5) or 3D\_ALG\_Ca  
402 (CER d18:1-22:0, CER d18:1-22:2, CER d18:1-22:5) compared to the respective support made with  
403 FeCl<sub>3</sub>. These findings suggest that, although the biomaterial and the geometry are the same, its surface  
404 morphology and the presence of Ca<sup>2+</sup> or Fe<sup>3+</sup> ions could significantly increase the production and the  
405 quali- and quantitative distribution of this class of compounds.

406 In addition, LC-MS/MS chromatograms revealed that ceramides exist as a balance mixture of two  
407 isomers (data not shown). In particular, two isomeric forms were observed for CER d18:1-16:0, CER

408 d18:1-20:0, CER d18:1-22:0, CER d18:1-22:1, CER d18:1-22:2, with one isomer predominating over  
409 the second isomer, regardless of the architecture of the scaffold and the gelling agent.

410

### 411 **3.4. LPC**

412 The most representative LPC monitored were 16:0, 18:0 and 18:1 in all samples, whereas the other  
413 species were present in much lower amount (Figure 6). LPC 16:0, LPC 18:0 and LPC 18:1 show a  
414 very similar relative expression level in all the tested conditions. On the other hand, many minor  
415 components of this class reveal significantly higher abundance when cells were grown on 2D\_ALG  
416 than on 3D\_ALG. This is the case for LPC 20:2, LPC 20:3, LPC 20:4, LPC 22:4, LPC 22:5 and LPC  
417 22:6, when the gelling agent was FeCl<sub>3</sub>, and for LPC 20:2, LPC 22:5 and LPC 22:6 when CaCl<sub>2</sub> was  
418 employed. Interestingly, the influence of the gelling agent was observed for LPC 18:2, LPC 20:4 and  
419 LPC 22:0, where higher abundance was observed in 3D\_ALG\_Ca than in 3D\_ALG\_Fe.

420 All together these findings suggest that, although the main LPC composition is maintained, both the  
421 gelling agent and the scaffold structure may somehow affect LPC distribution .

422 As previously, LPC were detected as two isomeric forms, but no significant differences were  
423 observed in terms of relative intensities between the two gelling media or scaffold geometries.

424

### 425 **3.5. LPA**

426 LPA are usually present at very low concentrations in cell membranes and their detection is  
427 challenging. Using the LC-MS/MS method here proposed, the most abundant lipid detected was the  
428 16:0 specie in all samples (Figure 7). The data collected for LPA showed that the relative trend of  
429 these lipids was generally maintained with some slight differences especially related to the geometry  
430 of the scaffold. A significant increase of abundance in 2D\_ALG\_Fe vs 3D\_ALG\_Fe was observed  
431 for LPA 17:0 and LPA 20:1, while statistical difference was not reached for LPA 22:0. Consistently,  
432 a trend towards increased expression on 2D\_ALG\_Ca and 2D\_ALG\_Fe compared to respective  
433 3D\_ALG was observed for LPA 18:0. The abundance of this lipid specie was also influenced by the

434 gelling agent, since an increase of expression in 2D\_ and 3D\_ALG\_Ca versus 2D\_ and 3D\_ALG\_Fe  
435 was observed, despite not statistically significant.

436

### 437 **3.6. FFA**

438 Among the detected FFA, the most abundant species were 20:0 and 22:0. No significant differences  
439 were observed in the general trend of FFA on the different supports (Figure 8). Only an increase in  
440 the expression level of two minor species (FA 20:4 and FA 22:1) was observed when cells were  
441 grown on 2D\_ALG\_Ca vs 3D\_ALG\_Ca. These data suggest that FFA are not susceptible of  
442 significant influence neither from the geometry nor from the gelling agent .

443

## 444 **4. Conclusions**

445 3D cell cultures can add unknown physiologically relevant aspects compared to 2D.

446 Here the behavior of fibroblasts as well as their lipid profile in contact with ALG systems was  
447 demonstrated to be influenced both by the architecture (2D or 3D) and the type of gelling agent .

448 2D\_ and 3D\_ALG were prepared by using two gelling agents (CaCl<sub>2</sub> or FeCl<sub>3</sub>), and characterized  
449 from a chemical-physical point of view through determination of the water content, swelling tests  
450 and mechanical resistance tests and from a morphological point of view through SEM analysis. The

451 water content determination has shown that ALG\_Fe had a slightly higher water content than ALG\_

452 Ca , i.e. 92% and 90% respectively. The mechanical resistance tests have shown that the ALG\_Ca

453 had a greater elasticity than ALG\_ Fe, which were extremely rigid. Thus, the former needed more

454 strength to break. The swelling tests carried out showed that ALG- Ca swell and expand up to 6h.

455 On the other hand, ALG\_Fe, showed this behavior only up to 2h. Finally, the average pore size of

456 scaffolds gelled with both solutions, was suitable for fibroblast (diameter ranging from 15 to 20

457 microns) adhesion and growth.

458 A LC-MS/MS targeted approach was exploited to investigate the effects of cell-biomaterial

459 interaction on the profile of selected lipids belonging to CER, LPC, LPA and FFA classes. The results

460 clearly indicate that significant differences exist in the distribution of CER species in the fibroblasts  
461 and that these differences are determined by activation through biomaterial interactions. LPC  
462 distribution exhibited some differences among samples, whereas LPA and FFA resulted in more  
463 constant trends.

464 Generally, cell-biomaterial engineered substrate interactions is strongly influenced by mechanical  
465 factors and cell membranes exhibit very different behaviors depending on the elasticity of the  
466 substrate microenvironment they are anchored. In the case of CER, as abundant bioactive signaling  
467 lipids present in the cell membrane, both the architecture and the gelling media affected the relative  
468 distribution of these species, playing a fundamental role in the organization of specific membrane  
469 regions. In the case of LPC, present as minor phospholipids in the cell membrane, our data suggests  
470 that the main parameter affecting their cell membrane lipid distribution is the scaffold architecture  
471 with a significant decrease in the relative expression levels of the species with higher chain length  
472 (C20 to C22) for 3D\_ALG compared to 2D\_ALG.

473 As a final conclusion, different ALG scaffolds have the capabilities to affect the relative distribution  
474 profile of the main cell membrane lipids and this aspect could result in changes in the cell membrane  
475 properties and in a variation of the cell biological functions (e.g. signaling).

476

#### 477 **Acknowledgements**

478 The Authors thank Dr. Ivana Lavota, Dr. Giorgia D'Andrea and Mr. Davide Dallatana for the  
479 excellent technical assistance.

480

#### 481 **References**

482 [1] N. Huebsch, D.J. Mooney, 2009. Inspiration and application in the evolution of biomaterials,  
483 Nature. 462 (2009) 426–432. <https://doi.org/10.1038/nature08601>.

- 484 [2] M. Mabrouk, H. Beherei, D. Das, Recent progress in the fabrication techniques of 3D scaffolds  
485 for tissue engineering, *Materials Science and Engineering:C*. 110 (2020) 110716.  
486 <https://doi.org/10.1016/j.msec.2020.110716>.
- 487 [3] P. Grabiec, 2012. Micro-and Nano-systems for Chemical/Bio-medical Analysis and Diagnostics.  
488 *Procedia Engineering*. 47 (2012) 1502-1505. <https://doi.org/10.1016/j.proeng.2012.09.437>.
- 489 [4] Xiao Zhang, Cui Song, Guanghui Ma, Wei Wei, Mechanical determination of particle–cell  
490 interactions and the associated biomedical applications, *J. Mater. Chem. B*. 6 (2018) 7129-7143.  
491 <https://doi.org/10.1039/C8TB01590B>.
- 492 [5] J.A. Sanz-Herrera, E. Reina-Romo, Cell-biomaterial mechanical interaction in the framework of  
493 tissue engineering: insights, computational modeling and perspectives, *International journal of*  
494 *molecular sciences*.12 (2011) 8217–8244. <https://doi.org/10.3390/ijms12118217>.
- 495 [6] S.F. Badylak, D.O. Freytes, T.W. Gilbert, Extracellular matrix as a biological scaffold material:  
496 Structure and function, *Acta Biomaterialia*. 5 (2009) 1–13.  
497 <https://doi.org/10.1016/j.actbio.2008.09.013>.
- 498 [7] P. Noutsi, E. Gratton, S. Chaieb, 2016. Assessment of Membrane Fluidity Fluctuations during  
499 Cellular Development Reveals Time and Cell Type Specificity. *PloS one*. 11(6),e0158313.  
500 <https://doi.org/10.1371/journal.pone.0158313>.
- 501 [8] N. Mitrousis, A. Fokina, M.S. Shoichet, Biomaterials for cell transplantation, *Nat. Rev. Mater*. 3  
502 (2018) 441–456. <https://doi.org/10.1038/s41578-018-0057-0>.
- 503 [9] F. O’Brien, B. Harley, I. Yannas, L. Gibson, The effect of pore size on cell adhesion in collagen-  
504 GAG scaffolds, *Biomaterials*.26 (2005) 433-441. DOI: 10.1016/j.biomaterials.2004.02.052.
- 505 [10] I.V. Yannas, D.S. Tzeranis, B.A. Harley, P.T. So, Biologically active collagen-based scaffolds:  
506 advances in processing and characterization, *Philosophical transactions. Series A, Mathematical,*  
507 *physical, and engineering sciences*. 368 (2010) 2123–2139. <https://doi.org/10.1098/rsta.2010.0015>.

508 [11] J.C. Ashworth, M. Mehr, P.G. Buxton, S.M. Best, R.E. Cameron, Optimising collagen scaffold  
509 architecture for enhanced periodontal ligament fibroblast migration, Journal of materials science.  
510 Materials in medicine. 29 (2018) 166. <https://doi.org/10.1007/s10856-018-6175-9>.

511 [12] K. Miyazaki, J. Oyanagi, D. Hoshino, S. Togo, H. Kumagai, Y. Miyagi, Cancer cell migration  
512 on elongate protrusions of fibroblasts in collagen matrix, Scientific reports. 9 (2019) 292.  
513 <https://doi.org/10.1038/s41598-018-36646-z>.

514 [13] B.A. Aderibigbe, B. Buyana, Alginate in Wound Dressings, Pharmaceutics. 10 (2018) 42.  
515 <https://doi.org/10.3390/pharmaceutics10020042>.

516 [14] S.H. Aswathy, U. Narendrakumar, I. Manjubala, 2020. Commercial hydrogels for biomedical  
517 applications, Heliyon.6(4),e03719. <https://doi.org/10.1016/j.heliyon.2020.e03719>.

518 [15] F. Abasalizadeh, S.V. Moghaddam, E. Alizadeh, E. Akbari, E. Kashani, S. Fazljou, M. Torbati,  
519 A. Akbarzadeh, Alginate-based hydrogels as drug delivery vehicles in cancer treatment and their  
520 applications in wound dressing and 3D bioprinting, Journal of biological engineering. 14 (2020) 8.  
521 <https://doi.org/10.1186/s13036-020-0227-7>.

522 [16] W.R. Gombotz, S. Wee, Protein release from alginate matrices, Advanced Drug Delivery  
523 Reviews. 31 (1998) 267–85. [https://doi.org/10.1016/S0169-409X\(97\)00124-5](https://doi.org/10.1016/S0169-409X(97)00124-5).

524 [17] A.D. Augst, H.J. Kong, D.J. Mooney, Alginate Hydrogels as Biomaterials, Macromolecular  
525 Bioscience. 6 (2006) 623–633. <https://doi.org/10.1002/mabi.200600069>.

526 [18] K.Y. Lee, D.J. Mooney, Alginate: Properties and biomedical applications, Progress in Polymer  
527 Science. 37 (2012) 106–126. DOI: 10.1016/j.progpolymsci.2011.06.003.

528 [19] C.K. Kuo, P.X. Ma, Ionically crosslinked alginate hydrogels as scaffolds for tissue engineering:  
529 Part 1. Structure, gelation rate and mechanical properties, Biomaterials.22 (2001) 511–521. DOI:  
530 10.1016/s0142-9612(00)00201-5.

531 [20] I. Machida-Sano, Y. Matsuda, H. Namiki, *In vitro* adhesion of human dermal fibroblasts on iron  
532 cross-linked alginate films, Biomedical materials.4 (2009) 025008. DOI: 10.1088/1748-  
533 6041/4/2/025008.

534 [21] K.Y. Lee, D.J. Mooney, Hydrogels for Tissue Engineering, *Chem. Rev.*101 (2001) 1869–1880.  
535 <https://doi.org/10.1021/cr000108x>.

536 [22] J. Bhasarkar, D. Bal, Kinetic investigation of a controlled drug delivery system based on alginate  
537 scaffold with embedded voids, *Journal of Applied Biomaterials & Functional Materials*. (2019).  
538 <https://doi.org/10.1177/2280800018817462>.

539 [23] A. Jagadeesh, G.G. Chaudhari, D.K. Bal, S. Patra, S. Ganguly, Enhancement of Solute Release  
540 From Chitosan Scaffold With Embedded Submillimeter Voids, *International Journal of Polymeric*  
541 *Materials and Polymeric Biomaterials*. 64 (2015) 134-139.

542 [24] M. Saccani, L. Parisi, C. Bergonzi, A. Bianchera, C. Galli, G.M. Macaluso, R. Bettini, L. Elviri,  
543 Surface modification of chitosan films with fibronectin fragment-DNA aptamer complex to enhance  
544 osteoblastic cell activity: A mass spectrometry approach probing evidence on protein behavior, *Rapid*  
545 *Commun Mass Spectrom*. 33 (2019) 336-342. <https://doi.org/10.1002/rcm.8335>.

546 [25] L. Bergamonti, C. Bergonzi, C. Graiff, P. Lottici, R. Bettini, L. Elviri, 3D printed chitosan  
547 scaffolds: A new TiO<sub>2</sub> support for the photocatalytic degradation of amoxicillin in water, *Water Res*.  
548 163 (2019) 114841.

549 [26] C.Y. Chen, C.J. Ke, K.C. Yen, H.C. Hsieh, J.S. Sun, F.H. Lin, 3D porous calcium-alginate  
550 scaffolds cell culture system improved human osteoblast cell clusters for cell therapy, *Theranostics*.  
551 5(2015) 643–655. <https://doi.org/10.7150/thno.11372>.

552 [27] C. Bergonzi, A. Di Natale, F. Zimetti, C. Marchi, A. Bianchera, F. Bernini, M. Silvestri, R.  
553 Bettini, L. Elviri, Study of 3D-printed chitosan scaffold features after different post-printing gelation  
554 processes, *Sci Rep*. 9 (2019) 362. doi: 10.1038/s41598-018-36613-8.

555 [28] L. Elviri, R. Foresti, C. Bergonzi, F. Zimetti, C. Marchi, A. Bianchera, F. Bernini, M. Silvestri,  
556 R. Bettini, Highly defined 3D printed chitosan scaffolds featuring improved cell growth, *Biomed*  
557 *Mater*. 12 (2017) 045009. doi: 10.1088/1748-605X/aa7692.

558 [29] C. Intini, L. Elviri, J. Cabral, S. Mros, C. Bergonzi, A. Bianchera, L. Flammini, P. Govoni, E.  
559 Barocelli, R. Bettini, M. McConnell, 3D-printed chitosan-based scaffolds: An *in vitro* study of human

560 skin cell growth and an *in-vivo* wound healing evaluation in experimental diabetes in rats.  
561 Carbohydrate polymers. 199 (2018) 593-602. doi: 10.1016/j.carbpol.2018.07.057.

562 [30] C. Manzoni, D.A. Kia, J. Vandrovцова, J. Hardy, N.W. Wood, P.A. Lewis, R. Ferrari, Genome,  
563 transcriptome and proteome: the rise of omics data and their integration in biomedical sciences,  
564 Briefings in Bioinformatics. 19 (2018) 286–302. <https://doi.org/10.1093/bib/bbw114>.

565 [31] A. Lovric, M. Granér, E. Bjornson, M. Arif, R. Benfeitas, K. Nyman, M. Ståhlman, M.O.  
566 Pentikäinen, J. Lundbom, A. Hakkarainen, R. Sirén, M.S. Nieminen, N. Lundbom, K. Lauerma, M.R.  
567 Taskinen, A. Mardinoglu, J. Boren, Characterization of different fat depots in NAFLD using  
568 inflammation-associated proteome, lipidome and metabolome, Scientific reports. 8 (2018) 14200.  
569 <https://doi.org/10.1038/s41598-018-31865-w>.

570 [32] A. Echard, D. Burgess, The Changing Lipidome during Cell Division, *Cell*. 156 (2014) 394-395.  
571 <http://dx.doi.org/10.1016/j.cell.2014.01.018>.

572 [33] Y.C. Kao, P.C. Ho, Y.K. Tu, I.M. Jou, K.J. Tsai, Lipids and Alzheimer's Disease, *Int. J. Mol.*  
573 *Sci.* 21 (2020) 1505. <https://doi.org/10.3390/ijms21041505>.

574 [34] D. Fontaine, S. Figiel, R. Felix, S. Kouba, G. Fromont, K. Mahéo, M. Potier-Cartereau, A.  
575 Chantome, C. Vandier, Roles of endogenous ether-lipids and associated PUFA in the regulation of  
576 ion channels and their relevance for disease, *The Journal of Lipid Research*. 61 (2020). doi:  
577 10.1194/jlr.RA120000634.

578 [35] F. Mollinedo, C. Gajate, Lipid rafts as signaling hubs in cancer cell survival/death and invasion:  
579 implications in tumor progression and therapy, *The Journal of Lipid Research*. (2020). doi:  
580 10.1194/jlr.TR119000439.

581 [36] A.C. Kendall, M.M. Koszyczarek, E.A. Jones, P.J. Hart, M. Towers, C. Griffiths, M. Morris, A.  
582 Nicolaou, Lipidomics for translational skin research: A primer for the uninitiated, *Experimental*  
583 *Dermatology*. 27 (2018) 721–728. <https://doi.org/10.1111/exd.13558>.

584 [37] H.C. Lee, T. Yokomizo, Applications of mass spectrometry-based targeted and non-targeted  
585 lipidomics, *Biochemical and Biophysical Research Communications*. 504 (2018) 576–581.  
586 <https://doi.org/10.1016/j.bbrc.2018.03.081>.

587 [38] M. Ohba, K. Saeki, T. Koga, T. Okuno, Y. Kobayashi, T. Yokomizo, Profiling of bioactive  
588 lipids in different dendritic cell subsets using an improved multiplex quantitative LC-MS/MS method,  
589 *Biochemical and Biophysical Research Communications*. 504 (2018) 562-568.  
590 <https://doi.org/10.1016/j.bbrc.2018.06.026>.

591 [39] C. Giles, R. Takechi, V. Lam, S. Dhaliwal, J. Mamo, Contemporary lipidomic analytics:  
592 opportunities and pitfalls, *Progress in Lipid Research*. 71 (2018) 86-100.  
593 <https://doi.org/10.1016/j.plipres.2018.06.003>.

594 [40] M.J. Choi, H.I. Maibach, Role of Ceramides in Barrier Function of Healthy and Diseased Skin,  
595 *Am J Clin Dermatol*. 6 (2005) 215–223. <https://doi.org/10.2165/00128071-200506040-00002>.

596 [41] H. Alrbyawi, I. Poudel, R.P. Dash, N.R. Srinivas, A.K. Tiwari, R.D. Arnold, R. Jayachandra  
597 Babu, Role of Ceramides in Drug Delivery, *AAPS PharmSciTech*. 20 (2019) 287.  
598 <https://doi.org/10.1208/s12249-019-1497-6>.

599 [42] Z. Hu, S. Nizzero, S. Goel, E.L. Hinkle, X. Wu, C. Li, M. Ferrari, H. Shen, 2020. Molecular  
600 targeting of FATP4 transporter for oral delivery of therapeutic peptide, *Science Advances*.  
601 6(14),eaba0145. DOI: 10.1126/sciadv.aba0145.

602 [43] Y.C. Yung, N.C. Stoddard, J. Chun, LPA receptor signaling: pharmacology, physiology, and  
603 pathophysiology, *Journal of lipid research*. 55 (2014) 1192–1214.  
604 <https://doi.org/10.1194/jlr.R046458>.

605 [44] G. Tigyi, Aiming drug discovery at lysophosphatidic acid targets, *British journal of*  
606 *pharmacology*. 161 (2010) 241–270. <https://doi.org/10.1111/j.1476-5381.2010.00815.x>.

607 [45] W. Drobnik, G. Liebisch, F.X. Audebert, D. Frohlich, T. Gluck, P. Vogel, G. Rothe. G. Schmitz,  
608 Plasma ceramide and lysophosphatidylcholine inversely correlate with mortality in sepsis patients,  
609 *The Journal of Lipid Research*. 44 (2003) 754-761. doi: 10.1194/jlr.M200401-JLR200.

610 [46] H.C. Tseng, C.C. Lin, L.D. Hsiao, C.M. Yang, Lysophosphatidylcholine-induced mitochondrial  
611 fission contributes to collagen production in human cardiac fibroblasts, The Journal of Lipid  
612 Research. 60 (2019) 1573-1589. doi: 10.1194/jlr.RA11900014.

613  
614  
615  
616  
617  
618  
619  
620  
621  
622  
623  
624  
625  
626  
627  
628  
629  
630  
631  
632  
633  
634  
635  
636  
637  
638  
639  
640  
641  
642  
643  
644  
645  
646  
647  
648  
649  
650  
651  
652  
653  
654

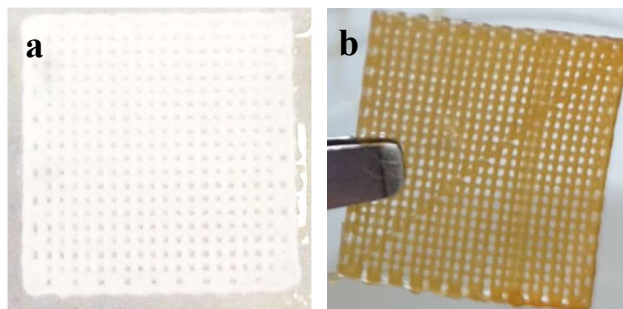
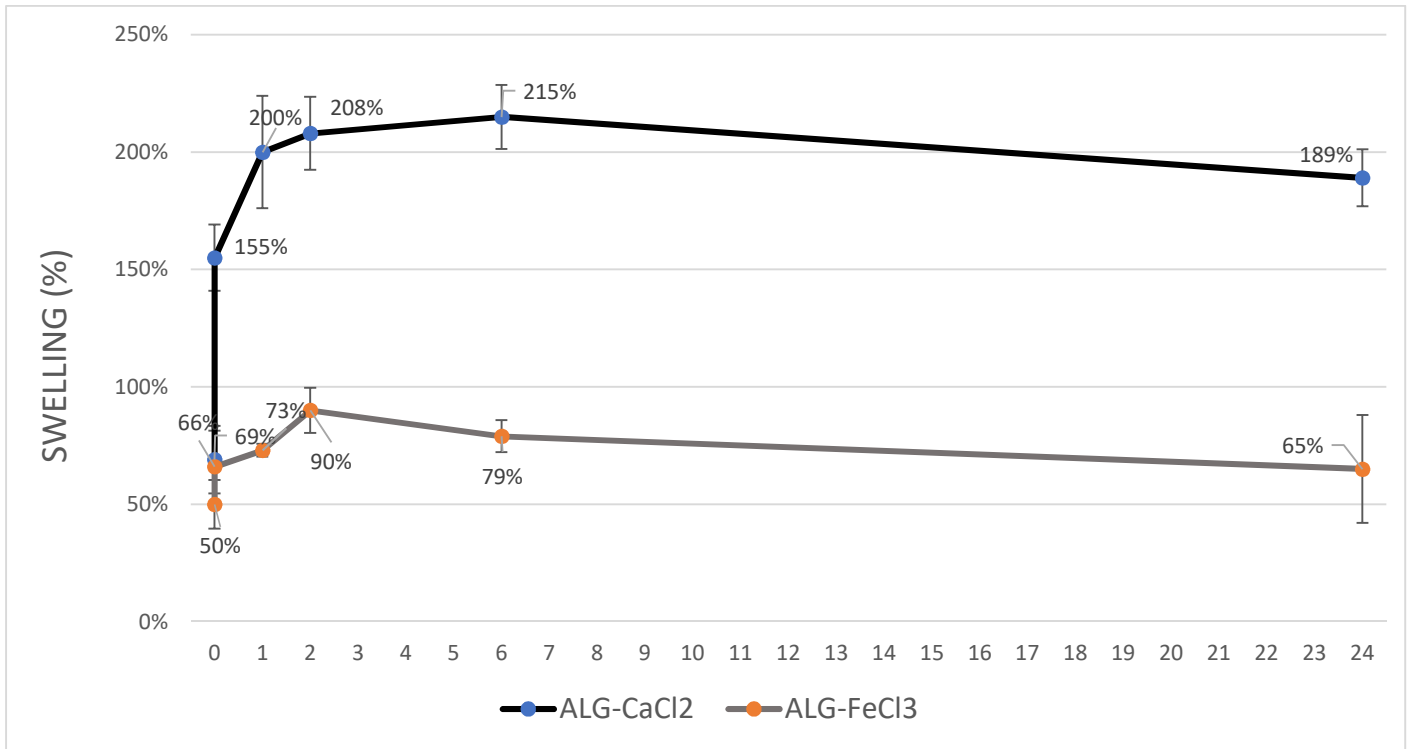


**Figure 1.** 3D printed alginate scaffolds gelled by: (a)  $\text{CaCl}_2$  and (b)  $\text{FeCl}_3$ .

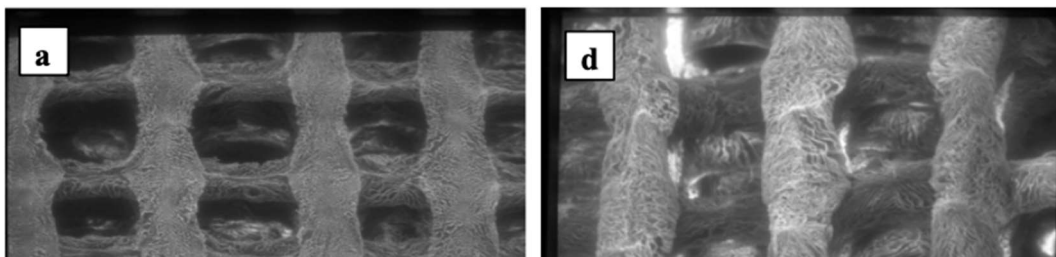
655  
656  
657  
658  
659  
660  
661  
662  
663  
664  
665  
666  
667  
668  
669  
670  
671  
672  
673  
674  
675  
676  
677  
678  
679  
680  
681  
682  
683  
684  
685  
686  
687  
688



689  
690  
691  
692  
693  
694  
695

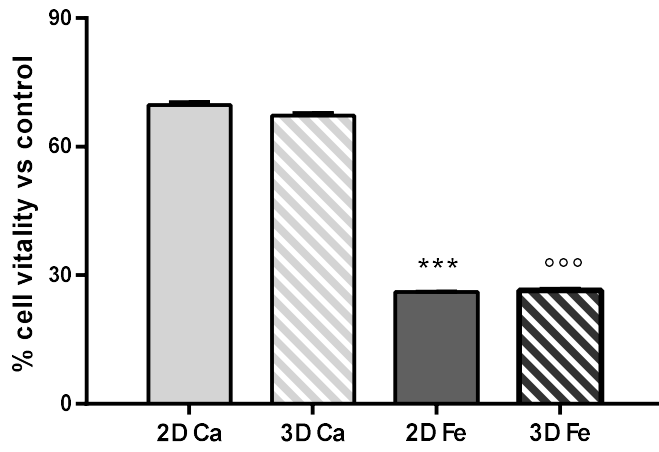
**Figure 2.** Swelling test of 3D\_ALG\_Ca (dark grey) and 3D\_ALG\_Fe (light grey) at different time point (n=5).

696  
697  
698  
699  
700  
701  
702  
703  
704  
705  
706  
707  
708  
709  
710  
711  
712  
713  
714  
715  
716



717  
718  
719  
720  
721  
722  
723  
724  
725  
726  
727  
728  
729  
730  
731  
732  
733  
734  
735  
736  
737  
738  
739  
740  
741  
742  
743  
744  
745  
746  
747  
748  
749  
750  
751  
752  
753  
754  
755  
756  
757  
758  
759  
760

**Figure 3.** SEM image of 3D\_ and 2D\_ ALG gelled with (a-c-g) CaCl<sub>2</sub> and (d-f-h) with FeCl<sub>3</sub> (4b). (a, b) 80X magnification; (b, e) 240X magnification; (c ) 640X magnification; (f) 320X magnification; (g, h) 300X magnification.

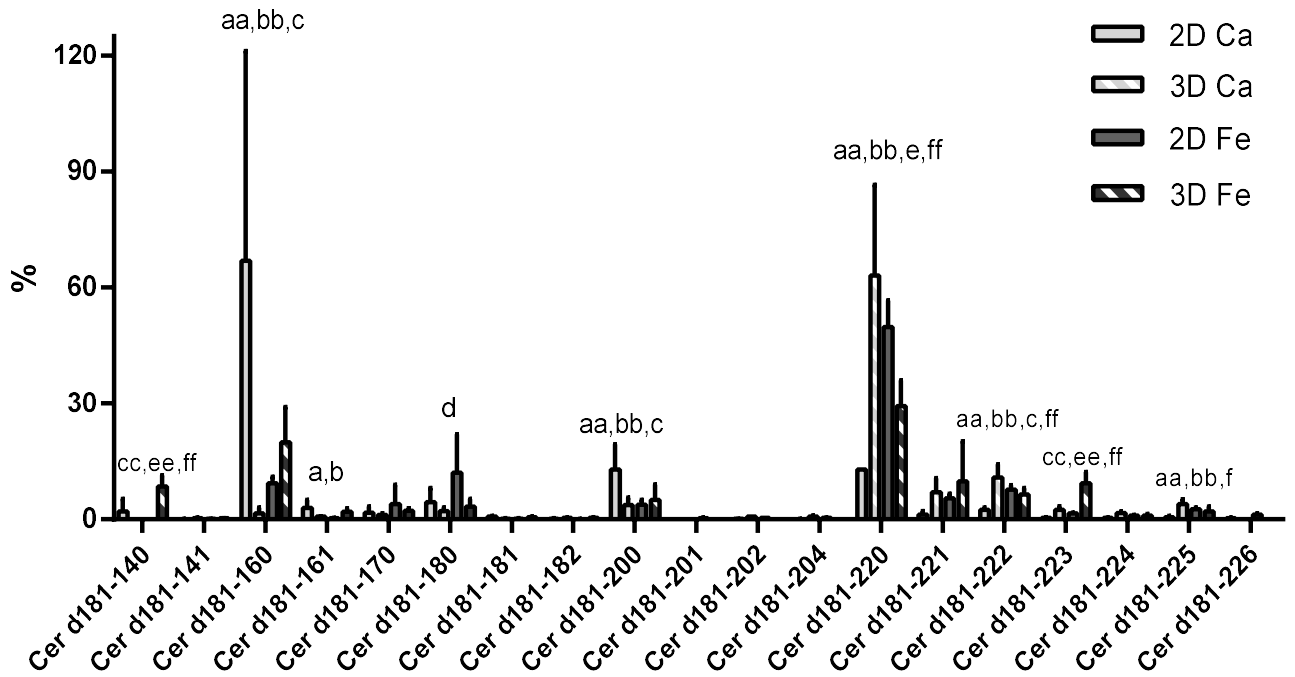


761

762 **Figure 4.** Cell vitality evaluated by MTT assay. \*\*\* $p < 0.001$  vs 2D Ca; ooo $p < 0.001$  vs 3D Ca.

763

764  
765  
766  
767  
768



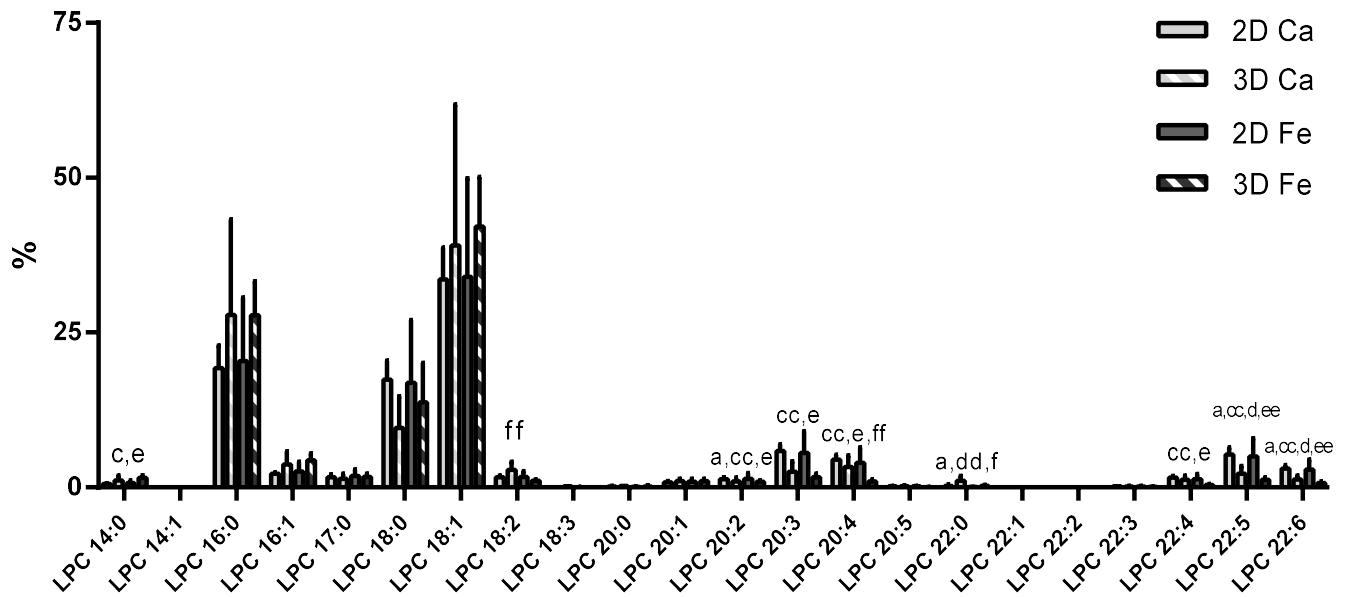
769  
770

771

772 **Figure 5.** Percentage abundance of ceramides in human fibroblast cells grown on 2D\_ and  
773 3D\_ALG\_Ca or 2D\_ and 3D\_ALG\_Fe . a:  $p < 0.05$  for 2D Ca vs 3D Ca, aa:  $p < 0.01$  for 2D Ca vs 3D  
774 Ca; b:  $p < 0.05$  for 2D Ca vs 2D Fe, bb:  $p < 0.01$  for 2D Ca vs 2D Fe; c:  $p < 0.05$  for 2D Ca vs 3D Fe,  
775 cc:  $p < 0.01$  for 2D Ca vs 3D Fe; d:  $p < 0.05$  for 2D Fe vs 3D Ca; e:  $p < 0.05$  for 2D Fe vs 3D Fe, ee:  
776  $p < 0.01$  for 2D Fe vs 3D Fe; f:  $p < 0.05$  for 3D Fe vs 3D Ca, ff:  $p < 0.01$  for 3D Fe vs 3D Ca.

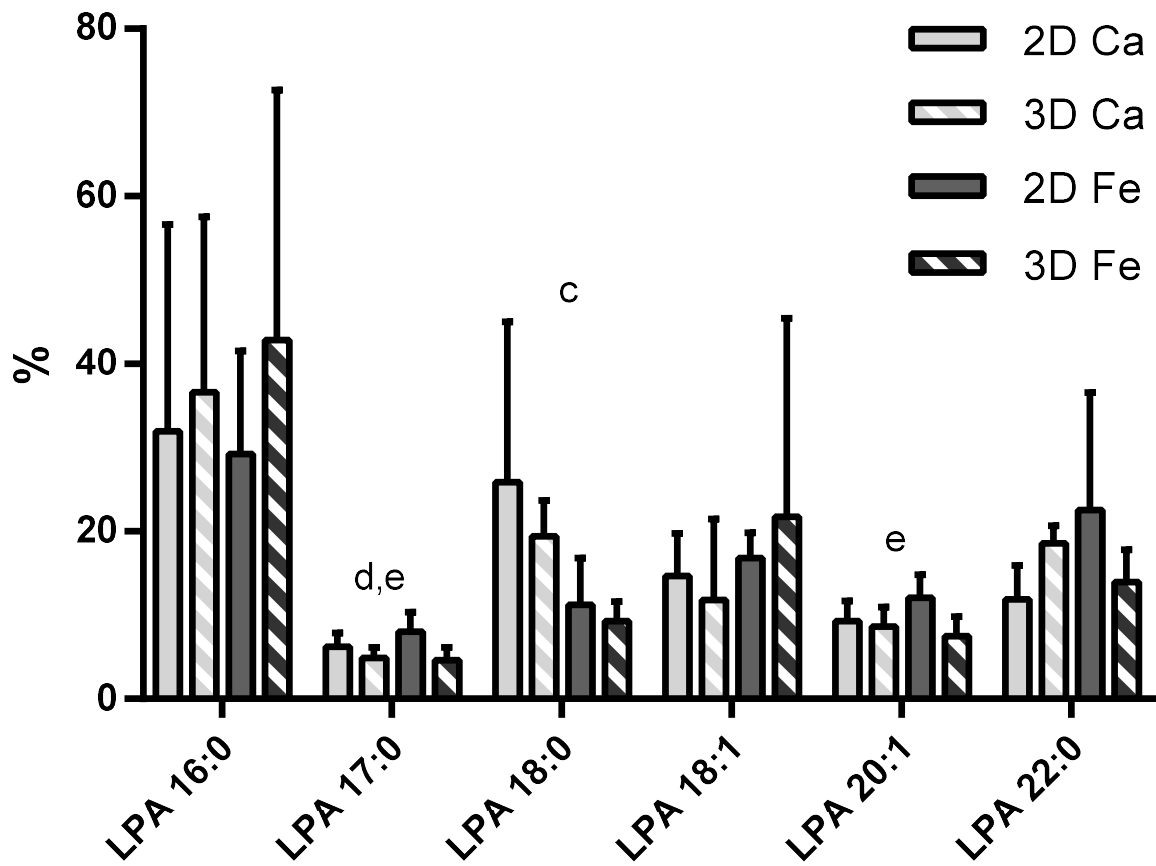
777  
778  
779  
780  
781  
782  
783  
784  
785

786  
787  
788  
789  
790  
791  
792  
793  
794



795  
796  
797  
798  
799  
800  
801  
802

**Figure 6.** Percentage abundance of LPCs in human fibroblast cells grown on 2D\_ and 3D\_ALG\_Ca or 2D\_ and 3D\_ALG\_Fe. a:  $p < 0.05$  for 2D Ca vs 3D Ca; c:  $p < 0.05$  for 2D Ca vs 3D Fe, cc:  $p < 0.01$  for 2D Ca vs 3D Fe; d:  $p < 0.05$  for 2D Fe vs 3D Ca; dd:  $p < 0.01$  for 2D Fe vs 3D Ca; e:  $p < 0.05$  for 2D Fe vs 3D Fe, ee:  $p < 0.01$  for 2D Fe vs 3D Fe; f:  $p < 0.05$  for 3D Fe vs 3D Ca, ff:  $p < 0.01$  for 3D Fe vs 3D Ca.



803  
 804  
 805 **Figure 7.** Percentage abundance of LPAs in human fibroblast cells grown on 2D\_ and 3D\_ALG\_Ca  
 806 or 2D\_ and 3D\_ALG\_Fe. c:  $p < 0.05$  for 2D Ca vs 3D Fe; d:  $p < 0.05$  for 2D Fe vs 3D Ca; e:  $p < 0.05$   
 807 for 2D Fe vs 3D Fe.

808

809

810

811

812

813

814

815

816

817

818

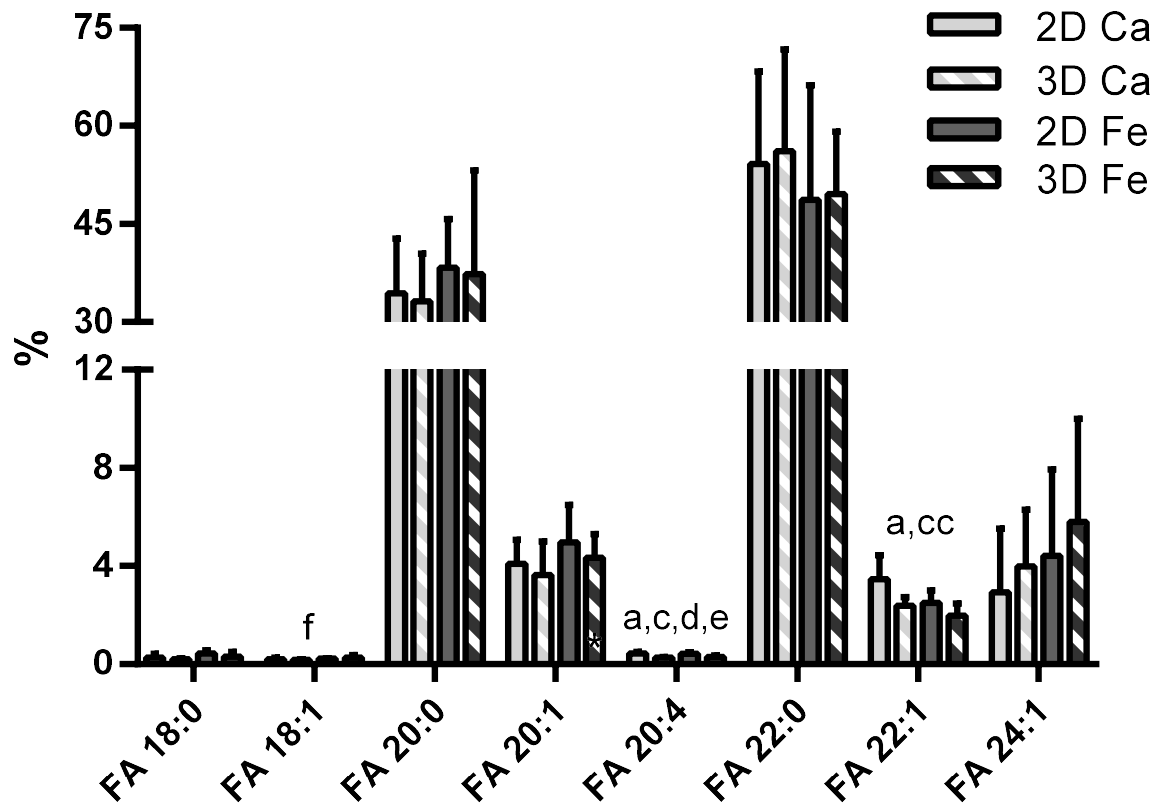
819

820

821

822

823  
824  
825



826  
827  
828  
829  
830  
831  
832  
833

**Figure 8.** Percentage abundance of FFAs in human fibroblast cells grown on 2D\_ and 3D\_ALG\_Ca or 2D\_ and 3D\_ALG\_Fe. a:  $p < 0.05$  for 2D Ca vs 3D Ca; c:  $p < 0.05$  for 2D Ca vs 3D Fe, cc:  $p < 0.01$  for 2D Ca vs 3D Fe; d:  $p < 0.05$  for 2D Fe vs 3D Ca; e:  $p < 0.05$  for 2D Fe vs 3D Fe.